JGR Space Physics

RESEARCH ARTICLE
10.1029/2025JA034016

# Simultaneous Observations of Quasi-Orthogonal Nighttime MSTIDs at Conjugate African-European Midlatitude Stations on 4 October 2018

**Zama T. Katamzi-Joseph[1,2], Carlos Martinis[3], Jonathan J. Makela[4], Yuichi Otsuka[5], John Bosco Habarulema[1,2,6], Alicreance Hiyadutuje[1], Shai Toledano[7], Mark B. Moldwin[7], and Jeffrey Baumgardner[3]**

[1]South African National Space Agency, Hermanus, South Africa, [2]Department of Physics and Electronics, Rhodes University, Makhanda, South Africa, [3]Center for Space Physics, Boston University, Boston, MA, USA, [4]Department of Electrical and Computer Engineering, University of Illinois Urbana-Champaign, Urbana, IL, USA, [5]Institute for Space-Earth Environmental Research, Nagoya University, Nagoya, Japan, [6]Centre for Space Research, Physics Department, North-West University, Potchefstroom, South Africa, [7]University of Michigan, Ann Arbor, MI, USA

**Key Points:**

- Conjugate and quasi-orthogonal nighttime medium-scale traveling ionospheric disturbances (MSTIDs) propagating equator-eastward and equator-westward observed in 630.0 nm airglow images
- Equator-eastward propagation was governed by background neutral winds through the wind filtering process
- Electric fields induced by gravity waves and sporadic E supported the development of two conjugate pairs of MSTIDs

**Supporting Information:**

Supporting Information may be found in the online version of this article.

**Correspondence to:**

Z. T. Katamzi-Joseph,
zkatamzi@sansa.org.za

**Citation:**

Katamzi-Joseph, Z. T., Martinis, C., Makela, J. J., Otsuka, Y., Habarulema, J. B., Hiyadutuje, A., et al. (2025). Simultaneous observations of quasi-orthogonal nighttime MSTIDs at conjugate African-European midlatitude stations on 4 October 2018. *Journal of Geophysical Research: Space Physics*, *130*, e2025JA034016. https://doi.org/10.1029/2025JA034016

Received 28 MAR 2025
Accepted 3 DEC 2025



**Abstract** Two quasi-orthogonal nighttime medium-scale traveling ionospheric disturbances (MSTIDs) were observed by conjugate midlatitude all-sky imagers in Sutherland (32.4°S, 20.8°E; magnetic latitude: ∼−40.9°) and Asiago (45.87°N, 11.53°E; magnetic latitude: ∼40.3°) on 4 October 2018. These MSTIDs had fronts elongated quasi-orthogonally to one another as observed from each location. The first MSTID was aligned northeast-southwest (NE-SW) in the Southern Hemisphere (SH) and northwest-southeast (NW-SE) in the Northern Hemisphere (NH) and propagated equator-westwards. These properties are typically attributed to MSTIDs generated through the coupled Perkins and sporadic E instabilities. This is supported by observed conditions in both hemispheres indicating the presence of sporadic E layers and reasonable Perkins instability growth rates. The second MSTID was aligned NW-SE (SH) and NE-SW (NH) and propagated equator-eastwards and represents the first optical observations of conjugate equator-eastward propagating MSTIDs. A possible linkage to gravity wave-induced polarization electric fields in the NH (and mapped to the SH) is presented, as significant gravity wave activity was observed in OH and OI greenline observations by the Asiago imager. Their equator-eastward propagation direction was favored by background winds at the hemisphere of origin, as determined from global model observations.

**Plain Language Summary** Observations of nighttime medium scale traveling ionospheric disturbances (MSTIDs) are reported in this study. MSTIDs are propagating plasma disturbances occurring in the ionospheric F region. The MSTIDs occurred simultaneously at conjugate locations in Sutherland, South Africa, and Asiago, Italy on the 4$^{th}$ of October 2018. The group of MSTID structures consisted of conjugate dark bands traveling equator-westwards and equator-eastwards. The former is a well-known characteristic of electrified MSTIDs (EMTIDs), while the latter presented a characteristic of nighttime conjugate MSTIDs that has not been reported before. The observed nighttime MSTIDs occurred concurrently with atmospheric gravity waves in the mesosphere, and sporadic E, which is a layer of thin sheet of enhanced plasma density that appear sporadically in the ionospheric E region. AGWs and sporadic E are known to generate polarization electric fields, which produce conducive conditions for the development of MSTIDs.

## 1. Introduction

Medium scale traveling ionospheric disturbances (MSTIDs) are wave- or band-like perturbations that are observed in plasma density, and other parameters of the ionosphere. They play a crucial role in atmospheric dynamics, including coupling between the different layers, and between conjugate hemispheres. On the other hand, they are seen as a threat to operational and scientific systems which either rely on the ionosphere (e.g., high frequency (HF) radio communication systems) or consider the ionosphere an inconvenience (e.g., radio telescopes and applications/systems based on global navigation satellite systems (GNSS)). This is because MSTIDs may introduce uncertainties in the predictability of these systems. For example, Zawdie et al. (2016) demonstrated that MSTIDs can introduce variability in the HF ray paths, which affects practical application of HF propagation. Also, Timote et al. (2020) showed that they cause degradation on the performance of differential positioning techniques used to determine accurate/precise positioning from GNSS.

Two-dimensional structures of nighttime MSTIDs have been observed in nighttime airglow images from highly sensitive charged coupled device (CCD) cameras (e.g., Garcia et al., 2000; Mendillo et al., 1997; Martinis et al., 2019; Otsuka et al., 2004) and total electron content maps from dense GNSS networks (e.g., Ding et al., 2011; Kotake et al., 2007; Otsuka et al., 2013). Nighttime MSTIDs have also been detected in satellite measurements as plasma density perturbations (e.g., Burke et al., 2016; Ding et al., 2011; Kotake et al., 2007) as well as localized fluctuations in the electric and magnetic fields, referred to as midlatitude magnetic field fluctuation and midlatitude electric field fluctuations, respectively (e.g., Park et al., 2016; A. Saito et al., 1995; Yokoyama & Stolle, 2017). Such studies reveal the following predominant general characteristics of nighttime MSTIDs (e.g., Burke et al., 2016; Martinis et al., 2019):

1. periods and wavelengths of 30–120 min and 100–500 km, respectively,
2. wavefronts that are aligned in the northwest-southeast (NW-SE) or northeast-southwest (NE-SW) in the Northern or Southern Hemisphere (SH), respectively, and that extend for a few thousand km,
3. propagate south-westward (north-westward) in the Northern (Southern) Hemisphere with speeds roughly between 50 and 300 m/s,
4. occur more frequently near the solstices than the equinoxes, and at low solar activity periods.

MSTIDs were originally thought to be manifestations of atmospheric gravity waves (AGWs) (Hines, 1960; Jacobson et al., 1995), but with extensive investigations some of them are understood to also develop through electrodynamic processes, such as the Perkins instability (Garcia et al., 2000; Otsuka et al., 2004). Nighttime midlatitude MSTIDs generated through the Perkins instability tend to be observed simultaneously at conjugate regions as well as concurrently with sporadic E (Burke et al., 2016; Wan et al., 2020). The Perkins instability is essentially an ionospheric plasma instability due to ionospheric conductivity and electric current perturbations (Hamza, 1999; Perkins, 1973). This instability results in the correct NW-SE/NE-SW alignment of the nighttime MSTIDs, but not the preferred propagation direction, and its growth rate is inefficient to generate MSTIDs (Kelley & Makela, 2001). As a result, coupling between E and F regions, specifically instabilities in the E region, has been suggested to overcome these shortfalls. E-F coupling mechanisms include gravity waves and sporadic E as sources through which polarization electric field could be enhanced, leading to plasma density fluctuations and the development of MSTIDs (Kelley et al., 2003; Makela & Otsuka, 2012; Tsunoda & Cosgrove, 2001). This was supported by observations and simulations which showed that quasi-periodic (QP) echoes associated with polarization electric field generated as a result of a non-uniform distribution of plasma structures within a sporadic E layer and/or wind fluctuations caused by gravity waves have the same directional preference as the Perkins instability and nighttime MSTIDs (Cosgrove & Tsunoda, 2004; Yokoyama et al., 2004). The MSTIDs generated through this mechanism are sometimes referred to as electrified MSTIDs (EMSTIDs).

We report on a case of unique observations of quasi-orthogonal MSTIDs that were detected in nighttime airglow images produced by conjugate midlatitude all-sky imagers (ASIs) on the 4$^{th}$ of October 2018. One pair of the conjugate structures consists of a NE-SW aligned dark band in the SH and a NW-SE aligned dark band in the Northern Hemisphere (NH) that propagated equator-westward. The other conjugate pair is a NW-SE aligned dark bank in the SH and a NE-SW aligned dark band in the NH with an equator-eastward propagation. While the conjugate equator-westward propagating MSTIDs seems to be a classic example of an EMSTID, the conjugate equator-eastward propagating pair has not been presented in literature before and therefore presents an interesting new case for further analysis. The observed structures are not related to disturbed geomagnetic conditions since Kp < 2 and SYM-H>-10 nT on this day.

## 2. Data and Method

Images of the atomic oxygen airglow emission at 630.0 nm (i.e., OI redline emission) from the Boston University ASIs in Sutherland, South Africa (32.4°S, 20.8°E; magnetic latitude: ∼−40.9°) and Asiago, Italy (45.87°N, 11.53°E; magnetic latitude: ∼40.3°) were used to analyze the nighttime MSTIDs under investigation in this study. The configuration of these ASIs is made up of a set lenses, including a wide angle fisheye lens, and a set of narrowband filters operating at wavelengths of 557.7, 605.0, 630.0, and 695.0 nm to isolate emissions from OI greenline, background/ambient, OI redline, and OH respectively. The Sutherland system has additional filters in wavelengths of 589.3 and 777.4 nm from Na, and OI, respectively. The detected photons are focused on a 1024 × 1024 CCD with 0.013 mm pixels. More details on the imaging system can be found in Martinis

**Table 1**
*Geographic Coordinates of the Ionosondes Used in This Study*

| URSI-code | Name | Latitude (°N) | Longitude (°E) |
|---|---|---|---|
| SO148 | Sopron | 47.63 | 16.72 |
| RO041 | Rome | 41.9 | 12.5 |
| LV12P | Louisvale | −28.5 | 21.2 |
| GR13L | Grahamstown | −33.3 | 26.5 |
| HE13N | Hermanus | −34.4 | 19.2 |

et al. (2018). Standard all-sky mapping processes were used to project the images onto a latitude/longitude grid assuming an emission layer at 250 km (e.g., Baumgardner et al., 2021; Garcia et al., 1997; Martinis et al., 2018, 2019). Airglow OI redline measurements were taken every ∼7 and 11 min at Asiago and Sutherland, respectively. A moving average over roughly 1 hr and spatial median filter across 7 pixels in longitude and latitude directions, corresponding to distances of 27 and 20 km in longitude and latitude, respectively, were applied to enhance the contrast in the MSTID structures with the background. According to the International Geomagnetic Reference Field (IGRF) model (Alken et al., 2021), the dip angle and magnetic declination of Sutherland are −63.9° and −23.1°, respectively, while these are 61.9° and 2.7°, respectively, at Asiago.

To investigate the influence of background neutral wind on the generation and propagation of the MSTIDs, we employed observations from a Fabry-Perot Interferometer (FPI) and the Horizontal Wind Model 2014 (HWM14). The FPI is co-located with the ASI in Sutherland, and provides neutral wind and temperature measurements from OI redline nighttime airglow. The instrument has an etalon with an air gap of 15 mm and partial reflectivity of approximately 77%. A narrowband interference filter (1 nm full width half maximum) centered at 630.0 nm with ∼55% transmission is placed in the optical path before the etalon to isolate the redline emission from other background emissions. The image is focused with an objective lens onto a 13.3 × 13.3 mm Andor CCD. This CCD chip has 1024 × 1024 pixels and is thermoelectrically cooled to below −60° to reduce dark noise. Above the optics sits a dual-mirror sky-scanning system that is driven by a smart motor on each axis, which allows for observations of the sky in any direction by rotating in elevation and azimuth. It operates in standard cardinal mode with elevation angle of 45°, pointing in the zenith, north, east, south, and west directions. Fisher et al. (2015) provides a detailed description of the instrument design and data processing. HWM14 model results are used in cases where FPI observations are not available, as is the case over Asiago. HWM14 is a widely used and readily available global empirical model that provides climatological neutral wind specifications, with predicted wind uncertainty in the range of about ±37 m/s (Drob et al., 2015). Midlatitude studies comparing the model's predictions to ground-truth FPI observations reported over or under estimation that ranged from about 20 m/s (Ojo et al., 2022) to 34 m/s (Fisher et al., 2015). Therefore, model errors were taken into account in our analysis of the wind's influence on the propagation of the observed MSTIDs.

Information on ionospheric variability, particularly sporadic E layer, was obtained from ionosondes located in proximity of the observed MSTIDs. These ionosondes are part of the global digisonde network under the Global Ionosphere Radio Observatory (Reinisch & Galkin, 2011). Each of these instruments consists of a transmitter that vertically transmit signals in the frequency range of 1–40 MHz and receivers that record time of flight of reflected signals. The output of the system is an ionogram, a plot that shows the height of the reflected signals, from which ionospheric characteristics, such as presence of sporadic E layer as well as its associated critical frequency, can be obtained. The locations of the ionosondes used in this study are provided in Table 1. Note that although San Vito (VT139; 40.6°N, 17.8°E) is also located within the field of view of the Asiago imager, this station did not have measurements during the night of this investigation. Ionosonde data cadence was 15 min.

Figure 1 shows the locations of the ASIs (blue "×"), FPI (red diamond) and its cardinal look direction positions (red "+"), and ionosondes (magenta triangle). The black circle in each map indicates the field of view of the ASI at 250 km and zenith angles below 80°.

## 3. Results and Discussions

Figure 2 shows orthogonal dark bands (representing low airglow intensity) extending NW-SE (dark band 1 (DB1)) and NE-SW (dark band (DB2)) while propagating north-eastward and north-westward, respectively. These dark bands were observed on the 4th of October 2018 with the Sutherland ASI and indicate a presence of MSTIDs. On this night, airglow observations began at approximately 17:23 and ended at 03:24 UT the following day. The north-eastward (i.e., equator-eastward) propagating MSTID was visible between roughly 20:07 and 23:52 UT, while the north-westward (i.e., equator-westward) propagating MSTID was observed at roughly 20:29–22:56 UT (see Movie S1 for raw images of this night at Sutherland). This means the equator-eastward and equator-westward propagating MSTIDs were observed for about 3.75 and 2.75 hr, respectively. Similar quasi-

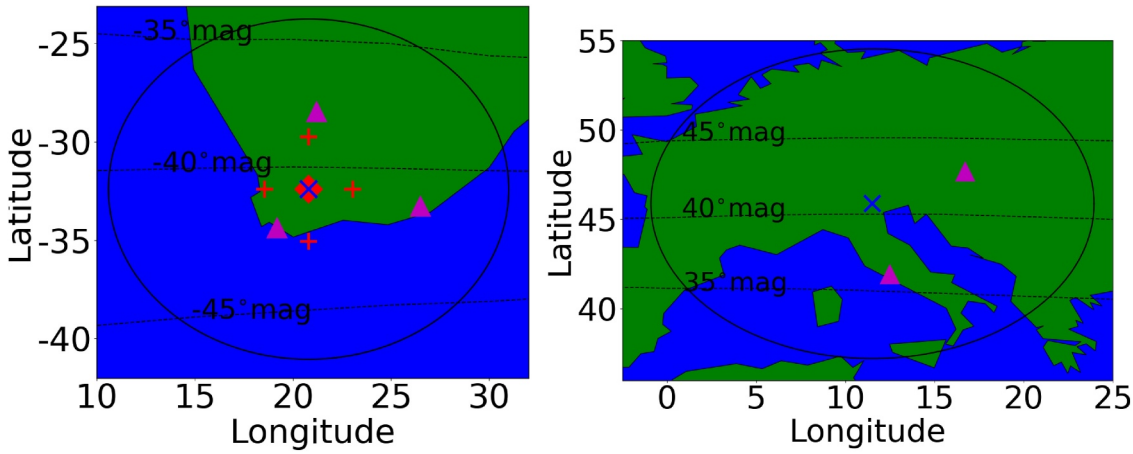


**Figure 1.** A map showing locations of the all-sky imagers (blue ×), Fabry-Perot Interferometer (FPI) (red diamond), FPI look directions (red +), and ionosondes (magenta triangle). The black circles represent the field of view at zenith angles less than 80° at a height of 250 km.

orthogonal dark band MSTIDs (same band alignment as in Sutherland), were also observed over Asiago as shown in Figure 3 (and Movie S2 showing raw images at Asiago). However, these MSTIDs were propagating in the southeast and southwest directions. While the airglow observations from the Asiago ASI were taken from 17:50 until 04:11 UT, the south-eastward (i.e., equator-eastward) propagating band was observed for about an hour at 21:30–22:33 UT, and the south-westward (i.e., equator-westward) propagating band for about 1.63 hr at 21:23–23:01 UT. These observations indicate that the MSTIDs started earlier and lasted longer in the SH compared to the NH. However, there is nearly 30 min of simultaneous observations of all MSTIDs in both hemispheres, while the equator-eastward propagating MSTIDs were observed simultaneously in both hemispheres for almost 1.5 hr.

To probe the mirroring of the MSTIDs structures, the Asiago images were mapped to the SH and the Sutherland images projected to the NH following the geomagnetic field lines using the IGRF-13 model. Both projections reveal the same information as they show clear correlation of MSTIDs in both hemispheres, and to avoid repetition we only present Sutherland images projected to the NH in Figure 4 (middle row). In this figure, the top row shows images taken by the Asiago ASI, while the bottom row shows a composite of images from both stations. Also, images taken almost at the same time at both stations are shown to illustrate and confirm magnetic conjugacy. In these images it can be seen that the phases of the wavefronts approximately match (see bottom row), cover almost the same area and propagate in the same directions. Therefore, these results show that MSTIDs

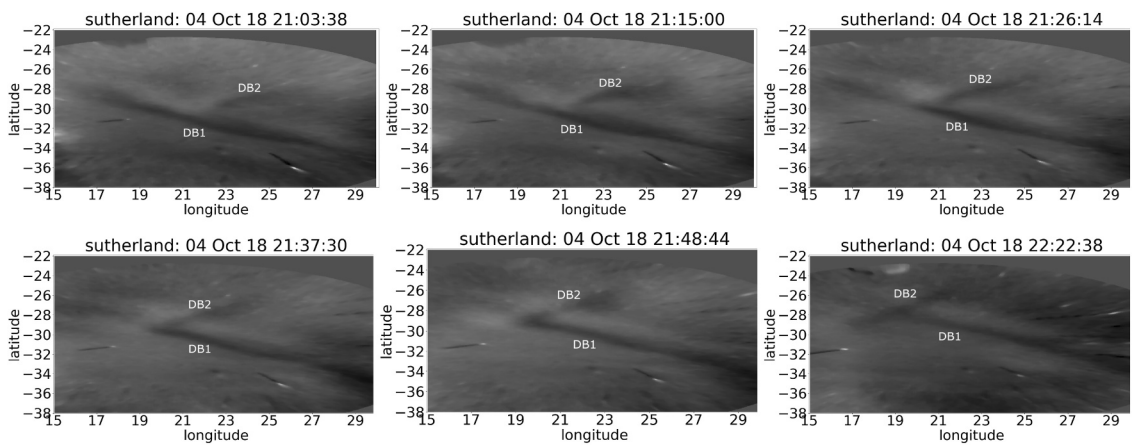


**Figure 2.** Nighttime airglow images showing dark band signatures of medium-scale traveling ionospheric disturbances (MSTIDs) observed by the Sutherland all-sky imager on the 4th of October 2018. DB1 and DB2 correspond to the dark bands 1 and 2, respectively. Time on the title of the plots is given in UT. See Movie S1 in the Supporting Information for dynamical evolution of these MSTIDs.

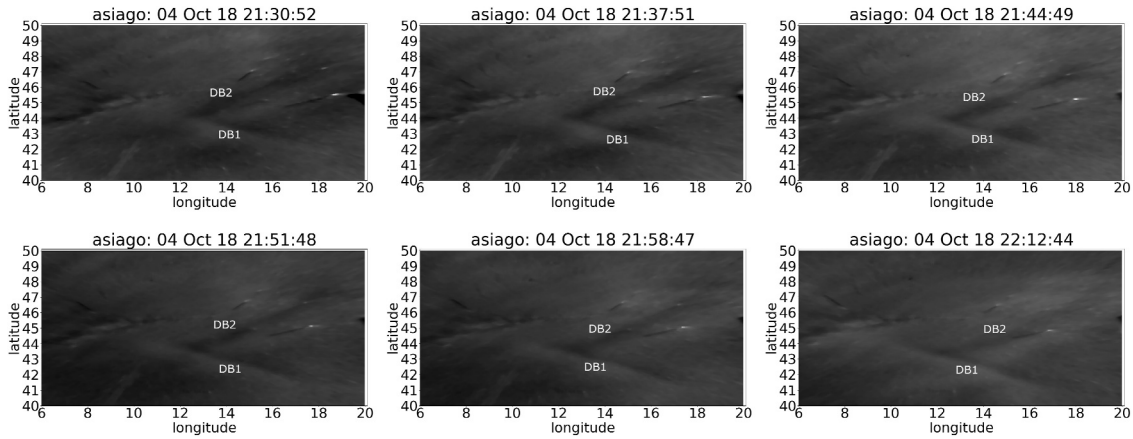


**Figure 3.** Same as in Figure 2 but for observations made by Asiago all-sky imager. See Movie S2 in the Supporting Information for dynamical evolution of these medium-scale traveling ionospheric disturbances.

structures are magnetic conjugate, which indicates that electric fields in the ionosphere may be involved with their occurrence.

The propagation properties of these MSTIDs were estimated from zonal and meridional keograms. These keograms are constructed from image slices along a particular latitude and longitude, respectively, at different epochs stacked together. Examples of the meridional (a and d) and zonal (b, c, e, and f) keograms used to calculate MSTID velocities are presented in Figure 5. The top rows shows the keograms derived from Asiago observations while the bottom are derived from the Sutherland observations. The magenta and red straight lines in the keograms indicate the equator-westward and equator-eastward propagating structures, respectively. A best-fit straight line is fitted on each dark band in the keograms and the slope of this line gives the speed of the MSTID in each horizontal component. The horizontal speed ($v_h$) and angle of propagation, that is, azimuth ($az$), were then calculated from the following equations (Martinis et al., 2019):

$$v_h = \frac{|v_z v_m|}{\sqrt{v_z^2 + v_m^2}}$$
$$az = \arctan\left(\frac{v_m}{v_z}\right) \quad (1)$$

where $v_z$ and $v_m$, are the speeds obtained from the zonal and meridional keograms, respectively. Several keograms at different latitudes/longitudes were constructed for each MSTID structure, which yielded a range of speeds and

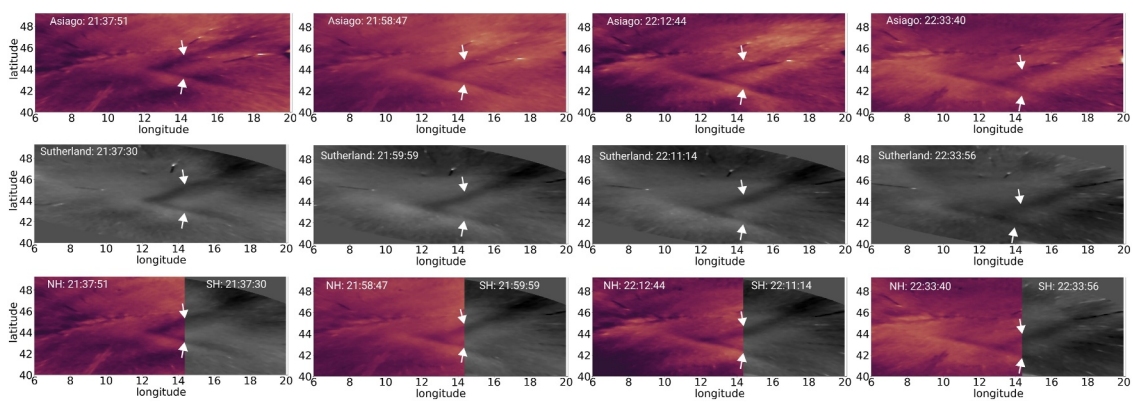


**Figure 4.** Simultaneous observations of medium-scale traveling ionospheric disturbances over Asiago (top row), Sutherland (middle row), and composite of Asiago and Sutherland images (bottom row). The Sutherland images are mapped to the Northern Hemisphere along the magnetic field lines.

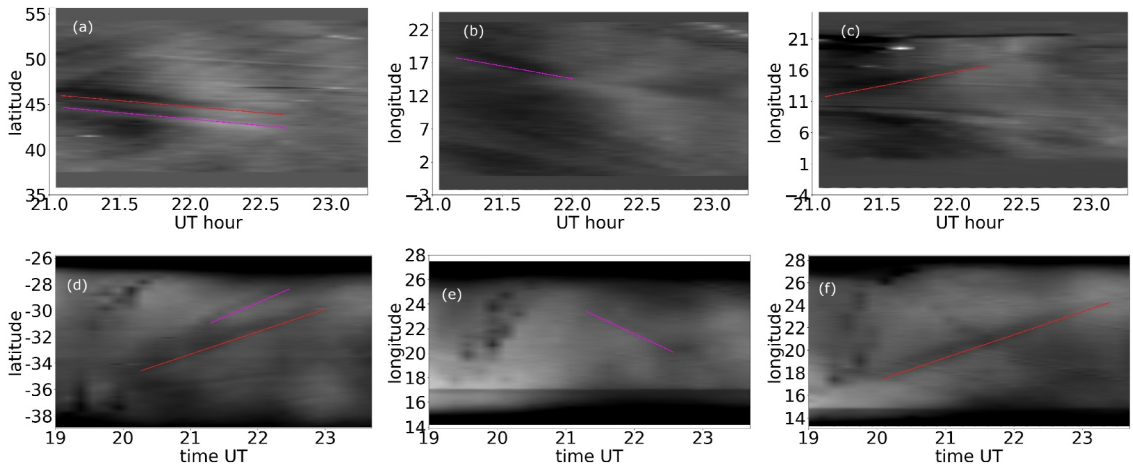


**Figure 5.** Examples of meridional and zonal keograms that were used to calculate propagation properties of the observed medium-scale traveling ionospheric disturbances (MSTIDs) on the 4th of October 2018. Top and bottom panels are keograms constructed from the Asiago and Sutherland, respectively. The red and magenta lines highlight wavefronts of the equator-eastward and equator-westward propagating MSTIDs, respectively. The keograms were constructed from measurements at longitudes 14°E (a), and 22°E (d) as well as latitudes 43.5°N (b), 46°N (c), 29°S (e), and 31°S (f).

azimuths from which the average and standard deviation were calculated to represent propagation characteristics of the MSTIDs. These characteristics are presented in Table 2, and reveal that the equator-eastward propagating MSTIDs have similar speeds, as do the equator-westward propagating MSTIDs, but with slightly greater speeds over Sutherland. The latter results agree with those found by Martinis et al. (2019) who also noted that the speeds of MSTIDs observed over Sutherland were greater than those of conjugate structures over Asiago. The difference in propagation azimuth between the two dark bands in each hemisphere is 85° and 88° for the Southern and Northern Hemispheres, respectively, confirming that the propagation directions of these MSTIDs are quasi-orthogonal. The propagation azimuth difference of the equator-westward propagating MSTIDs is about 86°, while that of the equator-eastward propagating MSTIDs is roughly 101°.

There have been many reported observations of conjugate nighttime MSTIDs propagating equator-westward, that is, south-westward and north-westward in the Northern and Southern Hemispheres, respectively (e.g., Burke et al., 2016; Martinis et al., 2019; Narayanan et al., 2018; Otsuka et al., 2004; Shiokawa et al., 2005). In their pioneering work Otsuka et al. (2004) explained the generation mechanisms for conjugate nighttime MSTIDs observations as involving polarization electric field at one hemisphere mapping to the opposite hemisphere along the magnetic field lines. This electric field, which is perpendicular to the wavefronts to maintain divergent free ionospheric currents, is directed in the east-west direction. Therefore, it would cause vertical movement of plasma through the E × B drifts, resulting in the dark (and bright) bands in the airglow images. This polarization electric field can be induced through processes involving gravity waves (Huang et al., 1994; Jonah et al., 2017) and/or sporadic E layer (Kelley et al., 2003; Narayanan et al., 2018; Otsuka et al., 2007).

As previously stated, the equator-westward propagating MSTID structures are generally accepted as being generated through a coupled mechanism involving Perkins instability and gravity waves and/or sporadic E. To explore whether there were suitable conditions for Perkins instability during the occurrence of the MSTIDs, the maximum Perkins instability growth rate ($\gamma_{\max}$) over the locations of our ASIs was computed using the following equation (Garcia et al., 2000):

**Table 2**
*Speeds and Azimuths of the Observed MSTIDs*

| | Asiago | | Sutherland | | $\Delta az$ (°) |
|---|---|---|---|---|---|
| | $v_h$ (m/s) | $az$ (°) | $v_h$ (m/s) | $az$ (°) | $\lvert az_A - az_S \rvert$ |
| MSTID 1 | 40 ± 3 | 236 ± 3 | 45 ± 2 | 322 ± 3 | 86 |
| MSTID 2 | 30 ± 2 | 148 ± 2 | 35 ± 3 | 47 ± 2 | 101 |

*Note.* A and S are abbreviations for Asiago and Sutherland, respectively.

$$\gamma_{\max} = \frac{1}{2H_n}\left[\frac{E_0}{B}\cos D + U_{s,mag}\cos D \sin D + U_{e,mag}\cos D \sin D\right] \quad (2)$$

where $H_n$ is the neutral scale height, $E_0$ is the electric field, $B$ is the magnetic field intensity, $D$ is the dip angle, $U_{s,mag} = U_e \sin\delta + U_s \cos\delta$ is the wind component in magnetic south, where $U_e$ and $U_s$ are the zonal eastward and meridional southward neutral wind components, respectively, $\delta$ is the magnetic declination, and $U_{e,mag} = U_e \cos\delta + U_s \sin\delta$ is the wind component

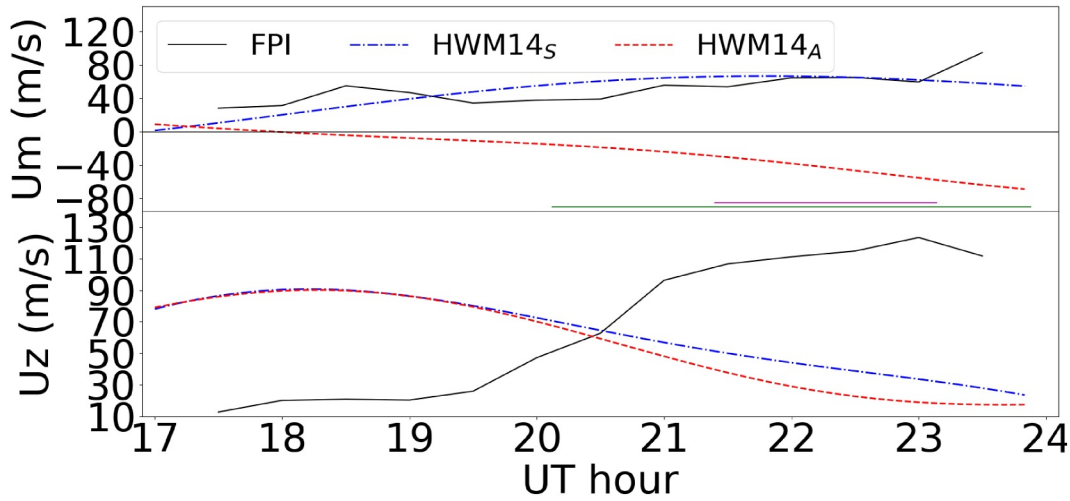


**Figure 6.** Meridional (Um) and zonal (Uz) thermospheric winds at 250 km over Sutherland and Asiago on the 4th of October 2018. The winds were obtained using Fabry-Perot Interferometer measurements at Sutherland (black solid line) and HWM14 predictions at Sutherland (blue dash dot line) and Asiago (red dash line). The green and magenta horizontal lines indicate time of observation of medium-scale traveling ionospheric disturbances over Sutherland and Asiago, respectively.

in magnetic east. For each location, the scale height was calculated using neutral parameters from NRLMSIS 2.0 (Emmert et al., 2020) and magnetic field parameters were obtained from IGRF-13. The neutral wind observations were obtained from the FPI co-located with the Sutherland ASI, and also from HWM14 for both Sutherland and Asiago as presented in Figure 6. In this figure, meridional (Um) and zonal (Uz) winds are positive northward and eastward, respectively. The winds are therefore equator-eastward over both locations on this night. Note that the modeled zonal winds (red and blue curves) seem phase shifted from the observed zonal wind (black curves). This was also found by Ojo et al. (2022) when they compared FPI and HWM14 winds over Sutherland and they attributed this to an incorrect estimation of the phase of the terdiurnal tide in HWM14. For the electric field we assumed threshold values of 1–3 mV/m as reasonable estimates for typical midlatitudes based on studies by A. Saito et al. (1995) and Narayanan et al. (2018). Using this information, the average maximum Perkins instability growth rates obtained were approximately 2–7 $\times$ $10^{-4}$ $s^{-1}$ for Sutherland and 3–6 $\times$ $10^{-4}$ $s^{-1}$ for Asiago. These values are reasonable for MSTIDs driven by Perkins instability based on prior studies (e.g., Garcia et al., 2000; Martinis et al., 2006).

The well-known problem though is that this growth is very small to efficiently generate MSTIDs (e.g., Kelley & Fukao, 1991; Kelley & Makela, 2001). However, Cosgrove and Tsunoda (2004) showed that the growth rate increases significantly when the Perkins instability is considered as a coupled system with sporadic E instability with the coupling driven by E-F electrodynamical processes. Sporadic E layers are known to occur simultaneously with nighttime MSTIDs and to have similar characteristics, for example, preferential front alignment and propagation direction as well as periodicity (e.g., Cosgrove & Tsunoda, 2003; Otsuka et al., 2007; S. Saito et al., 2007). They can be a source of polarization electric fields that may amplify Perkins instability via E-F coupling to induce equator-westward propagating MSTIDs. Figure 7 presents airglow images and ionograms to show examples where sporadic E was observed roughly simultaneous with MSTIDs on the 4th of October 2018 in the SH. The ionograms in this figure were produced by the Grahamstown and Louisvale ionosondes. In fact, sporadic E activity was recorded intermittently in all three ionosondes that are within the field of view of the Sutherland ASI prior to and during observations of the MSTIDs. Critical frequency of sporadic E ranged between 1.2 and 3.6 MHz throughout the night, while blanketing frequency of sporadic E was below 2.4 MHz, as shown by the top panel of Figure 8. It is noted that these frequencies are lower than those reported under similar circumstances, that is, simultaneous occurrence of sporadic E and conjugate MSTIDs (e.g., Narayanan et al., 2018; Sivakandan et al., 2022). This could be due to the longitudinal variation of sporadic E, which shows less activity in the African-European midlatitudes compared to other longitudes (Arras et al., 2008). In the NH, the two ionosondes that are within the field of view of the Asiago imager (i.e., Rome and Sopron) recorded intermittent sporadic E activity several hours prior to the MSTIDs observed in the NH. As can be seen from the bottom panel

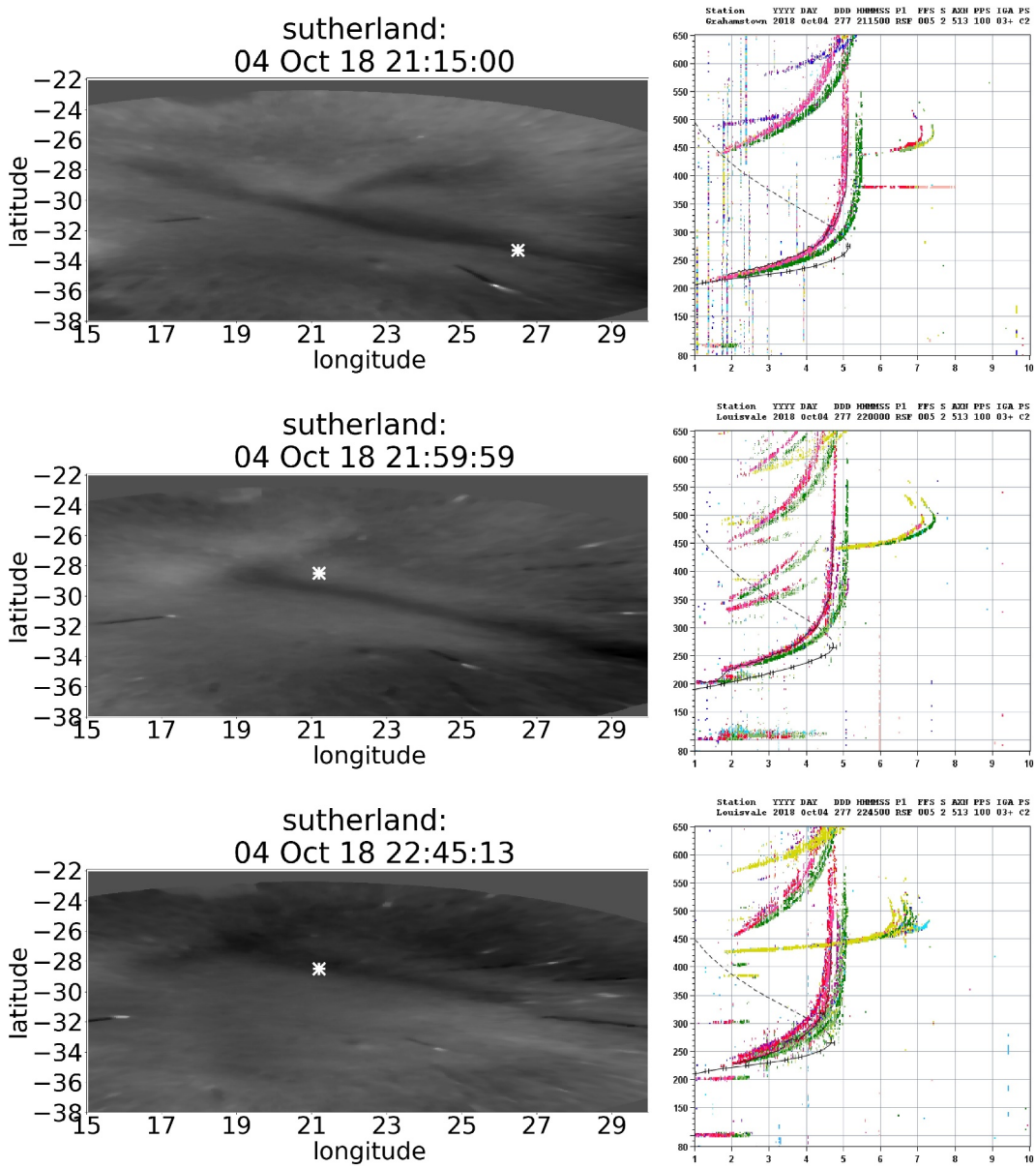


**Figure 7.** Examples of concurrent occurrences of medium-scale traveling ionospheric disturbances as observed by the Sutherland all-sky imager (left) and of sporadic E (at altitude around 90 km) as detected in ionograms from the Grahamstown and Louisvale ionosondes (right). The white asterisks in the images indicate the location of the ionosondes.

of Figure 8, sporadic E activity was recorded at 19:15–19:45 UT over Rome and intermittently between over 17:00 and 21:15 UT over Sopron. Critical and blanketing frequencies of sporadic E over these ionosondes were below 2.5 MHz, slightly lower than in the SH. However, unlike in the SH there was no coincidental observation of sporadic E and MSTIDs in the NH. Since sporadic E is observed prior to (SH and NH) and in conjunction with (SH) the equator-westward propagating MSTIDs, it is possible that sporadic E amplified Perkins instability and resulted in the conjugate MSTIDs. The coupled electrodynamic process involved in the development of these MSTIDs is presented in schematics of Figure 9a. This schematic diagram in Figure 9a shows the coupling between E and F regions, via the sporadic E layer and MSTIDs. Figure 9b presents coupling between lower atmosphere and ionosphere, through AGWs. Both schematics illustrate the coupling between the Southern and Northern Hemispheres through the magnetic field lines.

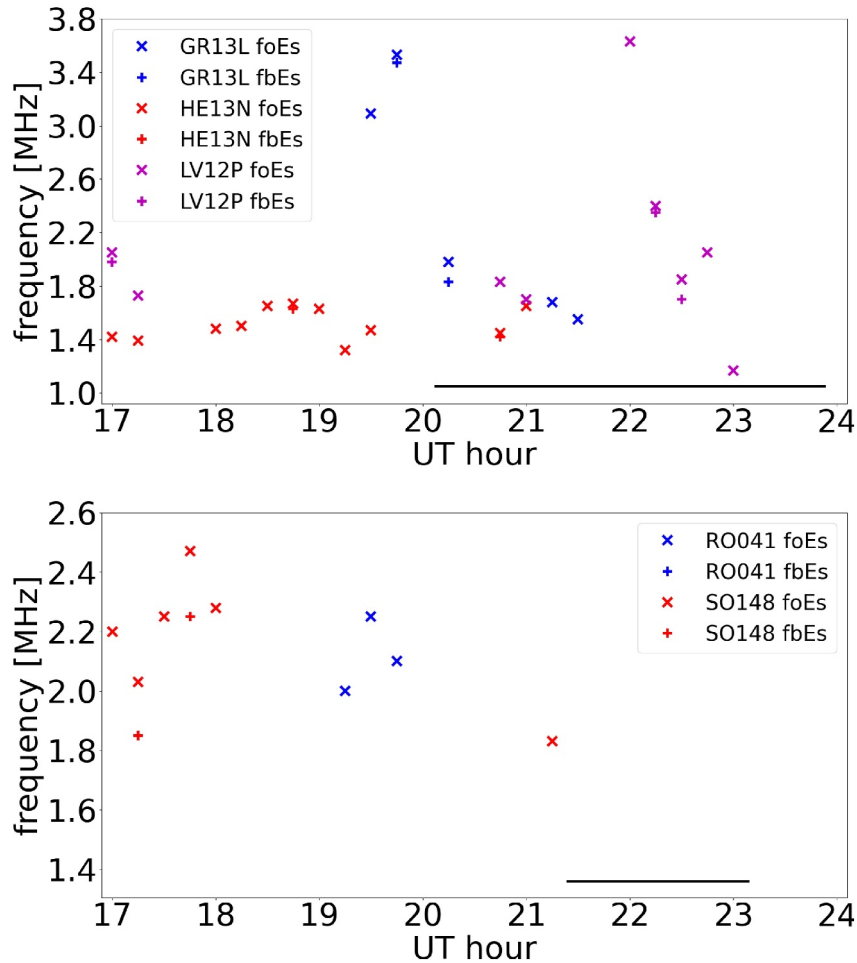


**Figure 8.** Critical (×) and blanketing (+) frequencies of sporadic E layer over Grahamstown (blue), Hermanus (red), and Louisvale in the top panel as well as over Rome (blue) and Sopron (red) in the bottom panel. The black horizontal line indicates the period over which medium-scale traveling ionospheric disturbances were observed in each hemisphere.

The optical observations of conjugate NE-SW (NH) and NW-SE (SH) aligned MSTID structures that are propagating equator-eastward are new and their geometry and propagation do not align with Perkins instability theory. However, they are probably also linked to electrodynamic coupling of both hemispheres driven by

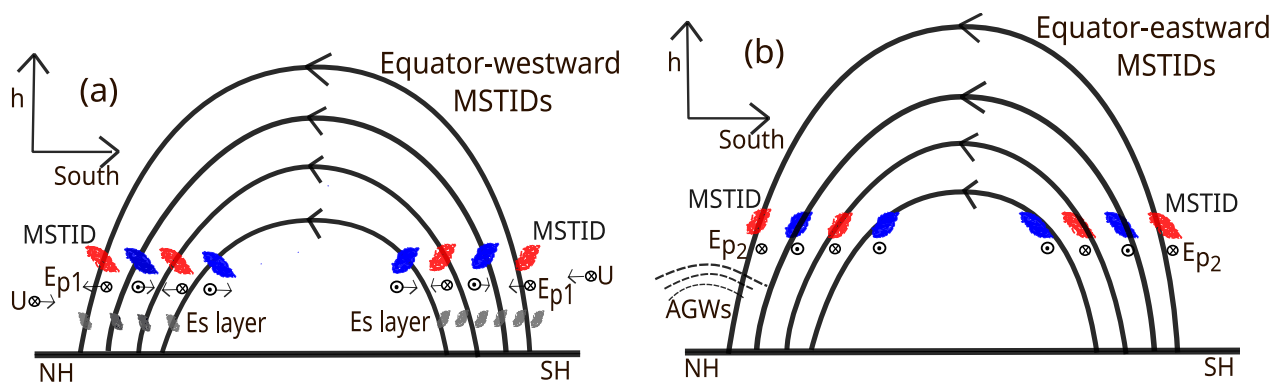


**Figure 9.** Schematic diagram of the dynamical and electrodynamical processes involved in the development of the observed equator-westward (a) and equator-eastward (b) medium-scale traveling ionospheric disturbances (MSTIDs). Note that (a) shows less sporadic E activity in the Northern Hemisphere compared to Southern Hemisphere, as per Figure 8 observations. Red and blue colors represents enhancements/bright bands and depletions/dark bands associated with MSTIDs.

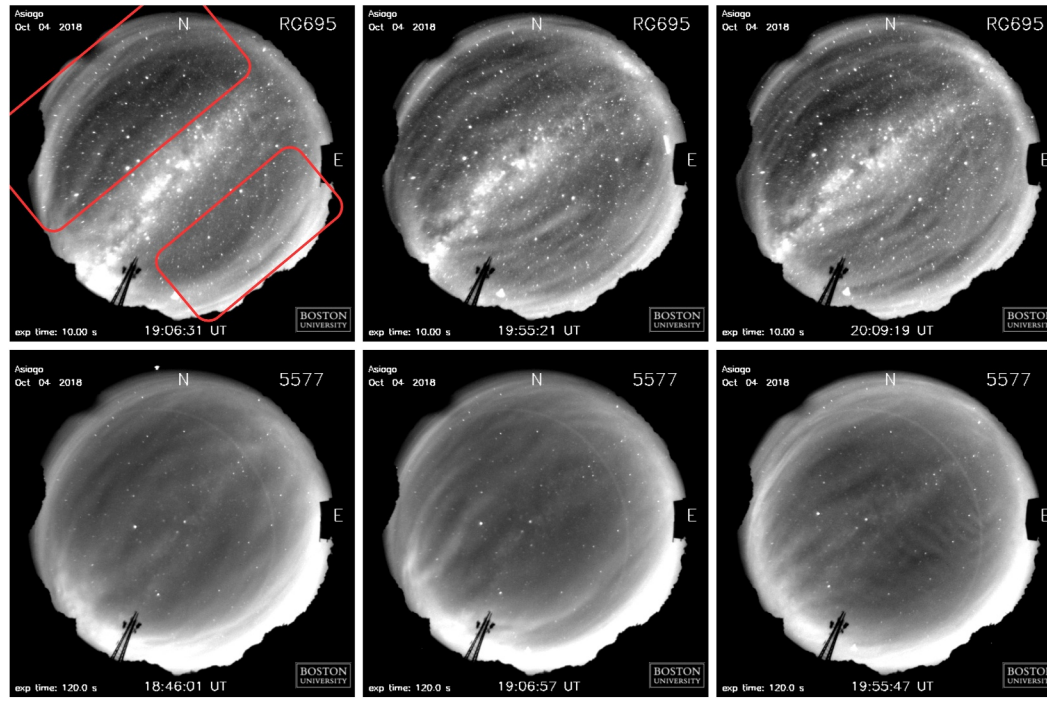


**Figure 10.** Raw images of the OH (top row) and OI greenline (bottom row) airglow observations taken by the Asiago imager. The red boxes are used to highlight signatures of gravity waves. Movies S3 and S4 in the Supporting Information show evolution of the OH and OI greenline observations, respectively.

polarization electric fields because of their simultaneous conjugate occurrence. As earlier stated, gravity waves are a possible source of polarization electric fields. Gravity waves are usually generated in the lower regions of the atmosphere, propagate toward the upper atmospheric layers where they dissipate in the lower thermosphere and generate secondary and tertiary waves (Vadas et al., 2009).

We checked for gravity wave activity using the Sutherland and Asiago imagers since they also take airglow measurements of atomic oxygen at 557.7 nm (OI greenline), sodium (Na) at 589.3 nm (only at Sutherland), and hydroxide (OH) at 695.0 nm, with peak emission altitude in the range of ∼85–95 km (i.e., mesosphere/lower thermosphere region). While the Sutherland ASI did not detect any gravity wave activity in any of the relevant three wavelengths, the Asiago imager did. Figure 10 presents sample images from the OH and OI greenline observations from which signatures of gravity waves were detected throughout the imager's field of view (see also Movies S3 and S4, respectively). Note, the bright NE-SW band in the OH images (top row) is the Milky Way galaxy. The gravity waves entered the field of view from the south-east and propagated toward the north-west, indicating that they were probably generated from a source located south of the imager. Analyses of the AGWs based on keograms (not shown here) revealed that the wavelengths of these waves are on the order of 10–40 km. On the other hand, based on the analysis of the keograms in Figure 5 the scale size (width) of the equator-eastward propagating MSTID observed in Asiago is roughly 117 ± 12 km. Since the AGWs and MSTIDs have different scale sizes, they may not be directly related. However, it is possible that secondary waves related to some of these gravity waves or acoustic waves reached thermospheric heights of ∼250 km, with the former propagating at an oblique vertical direction (e.g., Vadas & Crowley, 2010; Shinbori et al., 2023, and references therein). The winds associated with these acoustic-gravity waves could induced polarization electric fields since the perturbation winds drive currents through the magnetic field, via $\mathbf{J} = \sigma_p(\mathbf{U} \times \mathbf{B})$, where $\sigma_p$ is the Pedersen conductivity (Varney et al., 2009). Polarization electric field would be induced as long as the currents are not divergent-free. MSTIDs would then develop as the plasma is set in motion as a result of vertical E × B drift. Therefore, these results suggests that gravity waves in the NH produced conditions conducive to the development of conjugate equator-eastward propagating MSTIDs.

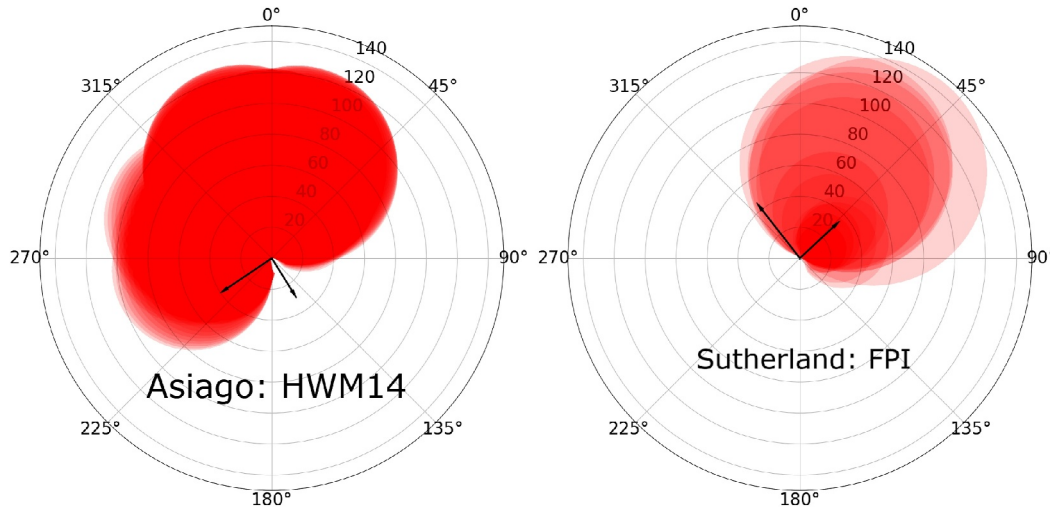


**Figure 11.** Wind blocking diagrams over Asiago and Sutherland for neutral wind at 250 km obtained from HWM14 (Asiago) and Fabry-Perot Interferometer (Sutherland).

The dynamical and electrodynamical processes involved in the development of the equator-eastward propagating MSTIDs are summarized in the schematics of Figure 9b. Observations of conjugate MSTIDs generated by electrodynamical processes driven by acoustic-gravity waves have been reported previously (e.g., Chou et al., 2022; Huba et al., 2015; Jonah et al., 2017; Shinbori et al., 2022). Simulations results presented by Huba et al. (2015) could reproduce MSTIDs results of Makela et al. (2011) for the 2011 Tohoku-Oki tsunami and clearly showed that electric field driven by tsunami induced gravity waves were responsible for conjugate ionospheric perturbations. Conjugate MSTIDs associated with this tsunami were later confirmed through observations presented by Chou et al. (2022). Furthermore, based on plasma flow perturbations from SuperDARN radar observations, Shinbori et al. (2022) were able to estimate that zonal electric field of the order of roughly 3 mV/m driven by neutral wind oscillations associated with atmospheric acoustic waves and AGWs linked to the 2022 Tonga volcanic eruption generated conjugate westward propagating MSTIDs over the Japan and Australian region. The MSTIDs detected in Makela et al. (2011), Chou et al. (2022), and Shinbori et al. (2022) propagated much faster (160–320 m/s) than those reported here. Also, those studies showed the conjugate MSTIDs propagated in a westerly direction, while in this case we show conjugate MSTIDs but with an eastern propagation. Furthermore, these studies (Chou et al., 2022; Shinbori et al., 2022) revealed very good spatial symmetry of the conjugate MSTIDs' wavefronts in both hemisphere, as has been observed in this study (see Figure 4). However, the AGWs that induced the polarization electric field associated with the conjugate MSTIDs in Huba et al. (2015), Chou et al. (2022), and Shinbori et al. (2022) were generated through natural hazards, meaning a lot of energy was put into the atmosphere, which is not necessarily the case in this study. Furthermore, past studies based on observations, and numerical or theoretical models reported that AGWs that are generated through normal meteorological processes, such as convection, topography, etc., can penetrate into the thermosphere/ionosphere and generate TIDs (e.g., Azeem & Barlage, 2018; Miyoshi et al., 2018; Vadas & Crowley, 2010). The source of AGWs presented in Figure 10 could not be identified in this study. Nonetheless, we postulate that the observed conjugate equator-eastward MSTIDs developed through AGW induced polarization electric field, though some order of magnitude smaller than previous reported cases, but models and/or simulations will be required to confirm this hypothesis.

The equator-eastward propagation direction of these MSTIDs can be explained by background wind filtering (Booker & Bretherton, 1967), as can be seen in Figure 11. The wind filtering process takes into account the Doppler-shifted frequency of gravity waves due to the horizontal wind, which is given by the following equation (Booker & Bretherton, 1967):

$$\Omega = \omega\left(1 - \frac{\mathbf{U}}{\mathbf{v}}\right) = \omega\left(1 - \frac{U_z \cos\phi + U_m \sin\phi}{\mathbf{v}}\right), \quad (3)$$

where $\omega$ is the source frequency, **U** is the horizontal wind speed with zonal and meridional components $(U_z, U_m)$, **v** is the horizontal phase velocity of the gravity wave. The red circles in Figure 11 indicate conditions where $\Omega \leq 0$, that is, where gravity wave-induced MSTIDs would be blocked due to their velocities being equal to the background wind at 250 km. To accommodate uncertainty in wind filtering analysis based on model data over Asiago, uncertainty in HWM14 winds were included in the computation of the blocking diagram over Asiago. From Fisher et al. (2015) and Jiang et al. (2018) we estimated that the maximum root mean square errors of HWM14 during October (same month as our case study) over the NH are roughly 34 and 32 m/s for meridional and zonal winds, respectively. Therefore, Figure 11 shows that background winds at 250 km support only the south-east propagation direction in the NH. Note that south-westward propagating MSTID over Asiago is unaffected by wind filtering in this case because this MSTID is generated by electrodynamic instability, as presented earlier, instead of dynamic perturbations. Similarly, Figure 11 (right plots) shows that the observed MSTIDs in the SH would have been blocked if they were generated through dynamic instead of electrodynamic processes.

Our results indicate that the NH had conditions conducive to the development of the equator-eastward MSTID. Therefore, why the MSTIDs would appear earlier in the conjugate hemisphere as seen in our observations is puzzling. One possibility is that the MSTIDs could have started earlier than observed by the Asiago ASI, but had very small amplitudes such that the imager was not sensitive enough to detect them from the beginning. However, as their amplitudes grew with time they were detectable later.

## 4. Conclusion

Simultaneous observations of two quasi-orthogonal and conjugate MSTIDs seen in the NH and SH on 4 October 2018 were presented. The two magnetically conjugate structures were observed in airglow images obtained from Sutherland (South Africa) and Asiago (Italy). One pair of MSTIDs was seen to propagate equator-westward, typical of MSTIDs associated with the Perkins instability and frequently reported in the literature. The second pair was seen to propagate equator-eastward, and represents the first such magnetically conjugate observations of an equator-eastward propagating MSTID. The MSTIDs observed from the SH appeared earlier (20:07–23:52 UT) and for longer than those seem from the NH (21:23–23:01 UT). However, the conjugate pairs traveled at similar speeds, albeit slightly faster in the SH. The conjugate occurrence of the two MSTIDs indicate that the structures were most likely induced through an electrodynamical coupling process, with electric fields generated in one hemisphere mapping to the other. The equator-westward propagating MSTID is attributed to the Perkins instability, the development of which was supported through the observed sporadic-E in both hemispheres. It is postulated that the generative mechanism for the unique equator-eastward propagating MSTIDs is lower atmospheric AGWs, which would induce electric fields that could map to the conjugate hemisphere. Coincident observations of AGWs in the NH combined with model results of background neutral wind filtering effects support this hypothesis. However, a complete simulation of these conditions remains to be done.

## Conflict of Interest

The authors declare no conflicts of interest relevant to this study.

## Data Availability Statement

Airglow ASI and Fabry-Perot Interferometer data are available at http://sirius.bu.edu/dataview/ and http://airglow.ece.illinois.edu/Data/Calendar. The ionosonde data were obtained through GIRO's DIDBase (https://ulcar.uml.edu/DIDBase/). NRLMSIS 2.0 and IGRF models were access via the Community Coordinated Modeling Center (CCMC) and World Data Center for Geomagnetism, Kyoto websites, that is, https://ccmc.gsfc.nasa.gov/models/NRLMSIS~2.0/ and https://wdc.kugi.kyoto-u.ac.jp/igrf/point/index.html, respectively.

**Acknowledgments**
This work is based on the research supported in part by the National Research Foundation of South Africa (reference CPRR23040389073). The work by MBM and ST were supported by NSF grants AGS1848724 and AGS2013433. The work by CM and JB was supported by NSF grant AGS2152365. CM acknowledges the continuing assistance from the personnel of the Asiago and Sutherland Observatories.

## References

Alken, P., Thébault, E., Beggan, C. D., Amit, H., Aubert, J., Baerenzung, J., et al. (2021). International geomagnetic reference field: The thirteen generation. *Earth Planets and Space*, *73*, 49. https://doi.org/10.1186/s40623-020-01288-x

Arras, C., Wickert, J., Beyerle, G., Heise, S., Schmidt, T., & Jacobi, C. (2008). A global climatology of ionospheric irregularities derived from GPS radio occultation. *Geophysical Research Letters*, *35*(14), L14809. https://doi.org/10.1029/2008GL034158

Azeem, I., & Barlage, M. (2018). Atmosphere-ionosphere coupling from convectively generated gravity waves. *Advances in Space Research*, *61*(7), 1931–1941. https://doi.org/10.1016/j.asr.2017.09.029

Baumgardner, J., Luettgen, S., Schmidt, C., Mayyasi, M., Smith, S., Martinis, C., et al. (2021). Long-term observations and physical processes in the Moon's extended sodium tail. *Journal of Geophysical Research: Planets*, *126*(3), e2020JE00667. https://doi.org/10.1029/2020JE006671

Booker, J., & Bretherton, F. (1967). The critical layer for internal gravity waves in a shear flow. *Journal of Fluid Mechanics*, *27*(3), 513–539. https://doi.org/10.1017/S0022112067000515

Burke, W. J., Martinis, C. R., Lai, P. C., Gentile, L. C., Sullivan, C., & Pfaff, R. F. (2016). C/NOFS observations of electromagnetic coupling between magnetically conjugate MSTID structures. *Journal of Geophysical Research: Space Physics*, *121*(3), 2569–2582. https://doi.org/10.1002/2015JA021965

Chou, M.-Y., Yue, J., Lin, C. C. H., Rajesh, P. K., & Pedatella, N. M. (2022). Conjugate effect of the 2011 tohoku reflected tsunami-driven gravity waves in the ionosphere. *Geophysical Research Letters*, *49*(3), e2021GL097170. https://doi.org/10.1029/2021GL097170

Cosgrove, R. B., & Tsunoda, R. T. (2003). Simulation of the nonlinear evolution of the sporadic-E layer instability in the nighttime midlatitude ionosphere. *Journal of Geophysical Research*, *108*(A7), 1283. https://doi.org/10.1029/2002JA009728

Cosgrove, R. B., & Tsunoda, R. T. (2004). Instability of the E-F coupled nighttime midlatitude ionosphere. *Journal of Geophysical Research*, *109*(A4), A04305. https://doi.org/10.1029/2003JA010243

Ding, F., Wan, W., Xu, G., Yu, T., Yang, G., & Wang, J. (2011). Climatology of medium-scale traveling ionospheric disturbances observed by a GPS network in central China. *Journal of Geophysical Research*, *116*(A9), A09327. https://doi.org/10.1029/2011JA016545

Drob, D., Emmert, J., Meriwether, J., Makela, J., Doornbos, E., Conde, M., et al. (2015). An update to the horizontal wind model (HWM): The quiet time thermosphere. *Earth and Space Science*, *2*(7), 301–319. https://doi.org/10.1002/2014ea000089

Emmert, J. T., Drob, D. P., Picone, J. M., Siskind, D. E., Jones, M. J., Mlynczak, M. G., et al. (2020). NRLMSIS 2.0: A whole-atmosphere empirical model of temperature and neutral species densities. *Earth and Space Science*, *7*(3), e2020EA001321. https://doi.org/10.1029/2020EA001321

Fisher, D. J., Makela, J. J., Meriwether, J. W., Benkhaldoun, Z., Kaab, M., & Lagheryeb, A. (2015). Climatologies of nighttime thermospheric winds and temperatures from Fabry-Perot interferometer measurements: From solar minimum to solar maximum. *Journal of Geophysical Research: Space Physics*, *120*(8), 6679–6693. https://doi.org/10.1002/2015JA021170

Garcia, F. J., Kelley, M. C., Makela, J. J., & Huang, C. S. (2000). Airglow observations of mesoscale low-velocity traveling traveling ionospheric disturbances at midlatitudes. *Journal of Geophysical Research*, *105*(A8), 18407–18415. https://doi.org/10.1029/1999JA000305

Garcia, F. J., Taylor, M. J., & Kelley, M. C. (1997). Two-dimensional spectral analysis of mesospheric airglow image data. *Applied Optics*, *36*(29), 7374–7385. https://doi.org/10.1364/AO.36.007374

Hamza, A. M. (1999). Perkins instability revisited. *Journal of Geophysical Research*, *104*(A10), 22567–22575. https://doi.org/10.1029/1999JA900307

Hines, C. O. (1960). Internal atmospheric gravity waves at ionospheric heights. *Canadian Journal of Physics*, *38*(11), 1441–1481. https://doi.org/10.1139/p60-150

Huang, C. S., Miller, C. A., & Kelley, M. C. (1994). Basic properties and gravity wave initiation of the midlatitude F region instability. *Journal of Geophysical Research*, *29*(1), 395–405. https://doi.org/10.1029/93RS01669

Huba, J. D., Drob, D. P., Wu, T. W., & Makela, J. J. (2015). Modeling the ionospheric impact of tsunami-driven gravity waves with SAMI3: Conjugate effects. *Geophysical Research Letters*, *42*(14), 5719–5726. https://doi.org/10.1002/2015GL064871

Jacobson, A. R., Robert, C. C., Massey, R. S., & Wu, G. (1995). Observations of traveling ionospheric disturbances with a satellite-beacon radio interferometer: Seasonal and local time behavior. *Journal of Geophysical Research*, *100*(A2), 1653–1665. https://doi.org/10.1029/94JA02663

Jiang, G., Xu, J., Wang, W., Yuan, W. S., Zhang, T. Y., Zhang, X., et al. (2018). A comparison of quiet time thermospheric winds between FPI observations and model calculations. *Journal of Geophysical Research: Space Physics*, *123*(9), 7789–7805. https://doi.org/10.1029/2018JA025424

Jonah, O. F., Kherani, E. A., & Paula, E. R. D. (2017). Investigations of conjugate MSTIDS over the Brazilian sector during daytime. *Journal of Geophysical Research: Space Physics*, *122*, 9576–9587. https://doi.org/10.1002/2017JA024365

Kelley, M. C., & Fukao, S. (1991). Turbulent upwelling of the mid-latitude ionosphere 2. Theoretical framework. *Journal of Geophysical Research*, *96*(A3), 3747–3753. https://doi.org/10.1029/90JA02252

Kelley, M. C., Haldoupis, C., Nicolls, M. J., Makela, J. J., Belehaki, A., Shalimov, S., & Wong, V. K. (2003). Case studies of coupling between the E and F regions during unstable sporadic-E conditions. *Journal of Geophysical Research*, *108*(A12), 1447. https://doi.org/10.1029/2003JA009955

Kelley, M. C., & Makela, J. J. (2001). Resolution of the discrepancy between experiment and theory of midlatitude F-region structures. *Geophysical Research Letters*, *28*(13), 2589–2592. https://doi.org/10.1029/2000GL012777

Kotake, N., Otsuka, Y., Ogawa, T., Tsugawa, T., & Saito, A. (2007). Statistical study of medium-scale traveling ionospheric disturbances observed with the GPS networks in southern California. Earth plan. *Space*, *59*(2), 95–102. https://doi.org/10.1186/BF03352681

Makela, J., Lognonné, L., Hébert, H., Rolland, L., Allgeyer, S., Kherani, A., et al. (2011). Imaging and modeling the ionospheric airglow response over Hawaii to the tsunami generated by the Tohoku earthquake of 11 March 2011. *Geophysical Research Letters*, *38*(24), L00G02. https://doi.org/10.1029/2011GL047860

Makela, J., & Otsuka, Y. (2012). Overview of nighttime ionospheric instabilities at low-and mid-latitudes: Coupling aspects resulting in structuring at the mesoscale. *Space Science Reviews*, *168*(1–4), 419–440. https://doi.org/10.1007/s11214-011-9816-6

Martinis, C., Baumgardner, J., Mendillo, M., Wroten, J., McDonald, T., Kosch, M., et al. (2019). First conjugate observations of medium-scale traveling ionospheric disturbances (TIDs) in the Europe-Africa longitude sector. *Journal of Geophysical Research: Space Physics*, *124*(3), 2213–2222. https://doi.org/10.1029/2018JA026018

Martinis, C., Baumgardner, J., Smith, S. M., Colerico, M., & Mendillo, M. (2006). Imaging science at El Leoncito, Argentina. *Annals of Geophysics*, *24*(5), 1375–1385. https://doi.org/10.5194/angeo-24-1375-2006

Martinis, C., Baumgardner, J., Wroten, J., & Mendillo, M. (2018). All-sky imaging capabilities for ionospheric space weather research using geomagnetic conjugate point observing sites. *Advances in Space Research*, *61*(7), 1636–1651. https://doi.org/10.1016/j.asr.2017.07.021

Mendillo, M., Baumgardner, J., Nottingham, D., Aarons, J., Reinisch, B., Scali, J., & Kelley, M. (1997). Investigations of thermosphere-ionospheric dynamics with 6300-Å images from the arecibo observatory. *Journal of Geophysical Research*, *102*(A4), 7331–7343. https://doi.org/10.1029/96JA02786

Miyoshi, Y., Jin, H., Fujiwara, H., & Shinagawa, H. (2018). Numerical study of traveling ionospheric disturbances generated by an upward propagating gravity wave. *Journal of Geophysical Research: Space Physics*, *123*(3), 2141–2155. https://doi.org/10.1002/2017JA025110

Narayanan, V. L., Shiokawa, K., Otsuka, Y., & Neudegg, D. (2018). On the role of thermospheric winds and sporadic E layers in the formation and evolution of electrified MSTIDs in geomagnetic conjugate regions. *Journal of Geophysical Research: Space Physics*, *123*(8), 6957–6980. https://doi.org/10.1029/2018JA025261

Ojo, T. T., Katamzi-Joseph, Z. T., Chu, K. T., Grawe, M. A., & Makela, J. J. (2022). A climatology of the nighttime thermospheric winds over sutherland, South Africa. *Advances in Space Research*, *69*(1), 209–219. https://doi.org/10.1016/j.asr.2021.10.015

Otsuka, Y., Onoma, F., Shiokawa, K., Ogawa, T., Yamamoto, M., & Fukao, S. (2007). Simultaneous observations of nighttime medium-scale traveling ionospheric disturbances and E region field-aligned irregularities at midlatitude. *Journal of Geophysical Research*, *112*(A6), A06317. https://doi.org/10.1029/2005JA011548

Otsuka, Y., Shiokawa, K., & Ogawa, T. (2004). Geomagnetically conjugate observations of medium-scale traveling ionospheric disturbances at midlatitude using all-sky airglow imagers. *Geophysical Research Letters*, *31*, L15803. https://doi.org/10.1029/2004GL020262

Otsuka, Y., Suzuki, K., Nakagawa, S., Nishioka, M., Shiokawa, K., & Tsugawa, T. (2013). GPS observations of medium-scale traveling ionospheric disturbances over Europe. *Annals of Geophysics*, *31*(2), 163–172. https://doi.org/10.5194/angeo-31-163-2013

Park, J., Lühr, H., Stolle, C., Rodriguez-Zuluaga, J., Knudsen, D. J., Burchill, J. K., & Kwak, Y.-S. (2016). Statistical survey of nighttime midlatitude magnetic fluctuations: Their source location and poynting flux as derived from the swarm constellation. *Journal of Geophysical Research: Space Physics*, *121*(11), 11235–11248. https://doi.org/10.1002/2016ja023408

Perkins, F. (1973). Spread F and ionospheric currents. *Journal of Geophysical Research*, *78*(1), 218–226. https://doi.org/10.1029/JA078i001p00218

Reinisch, B. W., & Galkin, I. A. (2011). Global ionospheric radio observatory (GIRO). Earth plan. *Space*, *63*(4), 377–381. https://doi.org/10.5047/eps.2011.03.001

Saito, A., Iyemori, T., Sugiura, M., Maynard, N., Aggson, T., Brace, L., et al. (1995). Conjugate occurrence of the electric field fluctuations in the nighttime midlatitude ionosphere. *Journal of Geophysical Research*, *100*(A11), 21439–21451. https://doi.org/10.1029/95JA01505

Saito, S., Yamamoto, M., Hashiguchi, H., Maegawa, A., & Saito, A. (2007). Observational evidence of coupling between quasi-periodic echoes and medium scale traveling ionospheric disturbances. *Annals of Geophysics*, *25*(10), 2185–2194. https://doi.org/10.5194/angeo-25-2185-2007

Shinbori, A., Otsuka, Y., Sori, T., Nishioka, M., Perwitasari, S., Tsuda, T., & Nishitani, N. (2022). Electromagnetic conjugacy of ionospheric disturbances after the 2022 Hunga Tonga–Hunga Ha'apai volcanic eruption as seen in GNSS-TEC and SuperDARN Hokkaido pair of radars observations. *Earth Planets and Space*, *74*(1), 106. https://doi.org/10.1186/s40623-022-01665-8

Shinbori, A., Otsuka, Y., Sori, T., Nishioka, M., Perwitasari, S., Tsuda, T., et al. (2023). New aspects of the upper atmospheric disturbances caused by the explosive eruption of the 2022 Hunga Tonga–Hunga ha'apai volcano. *Earth Planets and Space*, *75*(1), 175. https://doi.org/10.1186/s40623-023-01930-4

Shiokawa, K., Otsuka, Y., Tsugawa, T., Ogawa, T., Saito, A., Ohshima, K., et al. (2005). Geomagnetic conjugate observation of nighttime medium-scale and large-scale traveling ionospheric disturbances: FRONT3 campaign. *Journal of Geophysical Research*, *110*(A5), A05303. https://doi.org/10.1029/2004JA010845

Sivakandan, M., Martinis, C., Otsuka, Y., Chau, J. L., Norrell, J., Mielich, J., et al. (2022). On the role of E-F region coupling in the generation of nighttime MSTIDs during summer and equinox: Case studies over northern Germany. *Journal of Geophysical Research: Space Physics*, *127*(5), e2021JA030159. https://doi.org/10.1029/2021JA030159

Timote, C., Juan, J., Sanz, J., González-Casado, G., Rovira-García, A., & Escudero, M. (2020). Impact of medium-scale traveling ionospheric disturbances on network real-time kinematic services: CATNET study case. *Journal of Space Weather and Space Climate*, *10*, 29. https://doi.org/10.1051/swsc/2020030

Tsunoda, R. T., & Cosgrove, R. B. (2001). Coupled electrodynamics in the nighttime midlatitude ionosphere. *Geophysical Research Letters*, *28*(22), 4171–4174. https://doi.org/10.1029/2001GL013245

Vadas, S. L., & Crowley, G. (2010). Sources of the traveling ionospheric disturbances observed by the ionospheric TIDDBIT sounder near wallops island on 30 October 2007. *Journal of Geophysical Research*, *115*(A7), A07324. https://doi.org/10.1029/2009JA015053

Vadas, S. L., Taylor, M. J., Pautet, P.-D., Stamus, P. A., Fritts, D. C., Liu, H.-L., et al. (2009). Convection: The likely source of the medium-scale gravity waves observed in the OH airglow layer near Brasilia, Brazil, during the SpreadFEx campaign. *Annals of Geophysics*, *27*(1), 231–259. https://doi.org/10.5194/angeo-27-231-2009

Varney, R. H., Kelley, M. C., & Kudeki, E. (2009). Observations of electric fields associated with internal gravity waves. *Journal of Geophysical Research*, *114*(A2), A02304. https://doi.org/10.1029/2008JA013733

Wan, X., Xiong, C., Wang, H., Zhang, K., & Yin, F. (2020). Spatial characteristics on the occurrence of the nighttime midlatitude medium-scale traveling ionospheric disturbance at topside ionosphere revealed by the swarm satellite. *Journal of Geophysical Research: Space Physics*, *125*(8), e2019JA027739. https://doi.org/10.1029/2019JA027739

Yokoyama, T., Horinouchi, T., Yamamoto, M., & Fukao, S. (2004). Modulation of the midlatitude ionospheric E region by atmospheric gravity waves through polarization electric field. *Journal of Geophysical Research*, *109*(A12), A12307. https://doi.org/10.1029/2004JA010508

Yokoyama, T., & Stolle, C. (2017). Low and midlatitude ionospheric plasma density irregularities and their effects on geomagnetic field. *Space Science Reviews*, *206*(1–4), 495–519. https://doi.org/10.1007/s11214-016-0295-7

Zawdie, K. A., Drob, D. P., Huba, J. D., & Coker, C. (2016). Effect of time-dependent 3-D electron density gradients on high angle of incidence HF radiowave propagation. *Radio Science*, *51*(7), 1131–1141. https://doi.org/10.1002/2015RS005843